Supplementary Information

S1 Polarization Diffusion Model

The polarization evolution of a fiber link can be represented by a sequence of random unitary innovation matrices acting on the link Jones matrix. Following the stochastic polarization model established in coherent optical communication studies [1], the Jones matrix evolves recursively as

$$J_k = J(\dot{\vec{\phi}}_k)\, J_{k-1}, \tag{S1}$$

where the innovation matrix is

$$J(\dot{\vec{\phi}}_k) = \exp\left(-i\frac{\dot{\vec{\phi}}_k}{2} \cdot \vec{\sigma}\right), \tag{S2}$$

and $\vec{\sigma} = (\sigma_1, \sigma_2, \sigma_3)$ is the Pauli-matrix vector basis. The random increment vector obeys

$$\frac{\dot{\vec{\phi}}_k}{2} \sim \mathcal{N}\big(0,\, \sigma_p^2 I_3\big)\,, \tag{S3}$$

where $\sigma_p^2 = 2\pi \Delta p T$, $T = 1/F_s$ is the telemetry sampling interval, and Δp is the polarization linewidth in Hz. Each innovation matrix represents the accumulated birefringence perturbation contributed by a short fiber segment or a lumped optical element between telemetry samples. At low frequencies $f \ll F_s$, the cumulative effect of these i.i.d. increments produces a three-dimensional Brownian motion in the local tangent space of the polarization manifold, whose one-sided Power Spectral Density (PSD) follows

$$S_{\mathrm{pol}}(f) \approx \frac{\Delta p}{f^2}, \qquad f \ll F_s, \tag{S4}$$

consistent with the f^{-2} diffusion-dominated region observed in Figs. 3(a)–(f) of the main text. The discrete-time form used for spectral fitting is given in Methodology Eq. (5). The polarization diffusion strength σ_p^2 fitted from the measured PSDs provides a link-integrated measure of the accumulated birefringence fluctuations, and its dependence on cable length and architecture is discussed in the main text in the context of Fig. 3(h).

S2 Digital Signal Processing (DSP) Architecture Used in Simulations

The simulated coherent receiver consists of an optical front end followed by four DSP stages: static chromatic-dispersion compensation, a 2×2 butterfly adaptive time-domain equalizer, carrier phase recovery, and Jones-matrix telemetry extraction. The following subsections describe each stage and define the notation used throughout the supplementary material.

Received Signal Model

After coherent detection and Analog-to-Digital Converters (ADC) conversion, the dual-polarization received signal is represented as the discrete-time Jones vector

$$\mathbf{E}[m] = \begin{bmatrix} E_x[m] \\ E_y[m] \end{bmatrix}, \tag{S5}$$

where the index m runs over symbol periods. Following static chromatic-dispersion compensation in the frequency domain, the signal is fed into the butterfly equalizer.

Butterfly Equalizer

The 2×2 butterfly equalizer operates with four finite-impulse-response sub-filters $\mathbf{h}_{xx}$, $\mathbf{h}_{xy}$, $\mathbf{h}_{yx}$, and $\mathbf{h}_{yy}$, each of length $N+1$ taps. The equalizer output at symbol n is

$$E'_x(n) = \mathbf{h}_{xx}(n)^T E_x(n) + \mathbf{h}_{xy}(n)^T E_y(n), \tag{S6}$$

$$E'_y(n) = \mathbf{h}_{yx}(n)^T E_x(n) + \mathbf{h}_{yy}(n)^T E_y(n), \tag{S7}$$

where $E_x(n)$ and $E_y(n)$ denote length-$(N+1)$ vectors of received samples (with 2 samples per symbol) centered on symbol n.

Jones-matrix Extraction From Tap Sums

The zero-frequency tap sum of each sub-filter,

$$\overline{h}_{ij}^{(n)} = \sum_{m=0}^{N} h_{ij}^{(n)}[m], \tag{S8}$$

represents the zero-frequency response of that sub-filter and provides an estimate of the corresponding Jones-matrix element. The reconstructed 2×2 channel matrix is

$$\mathbf{H}_{\mathrm{DC}} = \begin{bmatrix} \overline{h}_{xx} & \overline{h}_{xy} \\ \overline{h}_{yx} & \overline{h}_{yy} \end{bmatrix}. \tag{S9}$$

This matrix is exported as telemetry at each observation period $T = 1/F_s$.

Decision-directed Least-Mean-Square (LMS) update

The sub-filter coefficients are updated using a decision-directed LMS rule:

$$\mathbf{h}_{k,l}(n+1) = \mathbf{h}_{k,l}(n) + \mu_h \, e_{hk}(n) \, \mathbf{E}_l(n)^*, \tag{S10}$$

where $k, l \in \{x, y\}$ index the output and input polarizations, respectively, μ_h is the equalizer step-size parameter, and $e_{hk}(n)$ is the decision-directed error signal for output polarization k at symbol n.

Carrier Phase Recovery

Carrier-Phase Estimation (CPE) is performed independently for each polarization using a gradient-descent phase tracker following the technique in [2]:

$$f_{x,y}(n+1) = f_{x,y}(n) + \frac{\mu_f}{\left|E'_{x,y}(n)\right|^2 + \epsilon}\, e_{f x,y}(n)\, E'_{x,y}(n)^*, \tag{S11}$$

where μ_f is the CPE step-size parameter and ϵ is a small regularization constant. In the joint CPE architecture, a common phase estimate is formed by averaging the two independent phase estimates:

$$f_{\text{ave}}(n) = \frac{f_x(n) + f_y(n)}{2}. \tag{S12}$$

This common correction is then applied to both polarizations, preserving the relative phase between tributaries and suppressing the artificial differential drift analyzed in Supplementary Note S4.

S3 Absolute Rotation Extraction From the Jones Matrix

To isolate the pure polarization rotation from the equalizer-derived Jones matrix $\mathbf{H}_{\text{DC}}$, Singular Value Decomposition (SVD) is first applied:

$$\mathbf{H}_{\text{DC}} = V\,\Sigma\,U^\dagger, \tag{S13}$$

where V and U are unitary matrices and Σ is a diagonal matrix of singular values. The unitary component of the channel matrix, which captures the polarization rotation while suppressing Polarization-Dependent Loss (PDL) encoded in the singular values, is extracted as

$$U_{\text{init}} = V\,U^\dagger. \tag{S14}$$

The common global optical phase is then removed by normalizing U_{init} into $SU(2)$:

$$U' = \frac{U_{\text{init}}}{\sqrt{\det(U_{\text{init}})}} = \begin{bmatrix} u_{11} & u_{12} \\ u_{21} & u_{22} \end{bmatrix}. \tag{S15}$$

The corresponding Stokes vector on the Poincaré sphere is

$$\vec{S} = \begin{bmatrix} |u_{11}|^2 - |u_{21}|^2 \\ 2\,\Re(u_{11}\,u_{21}^*) \\ 2\,\Im(u_{11}\,u_{21}^*) \end{bmatrix}. \tag{S16}$$

The absolute rotation vector in Stokes space is then obtained from the unit quaternion representation of U'. Writing the $SU(2)$ matrix as

$$U' = \begin{bmatrix} \alpha & -\beta^* \\ \beta & \alpha^* \end{bmatrix}, \qquad |\alpha|^2 + |\beta|^2 = 1, \tag{S17}$$

the four quaternion components are identified as

$$q_0 = \Re(\alpha), \quad q_1 = \Im(\alpha), \quad q_2 = \Re(\beta), \quad q_3 = \Im(\beta). \tag{S18}$$

The absolute rotation angle φ and rotation axis $\hat{\varphi}$ follow from

$$q_0 = \cos\left(\frac{\varphi}{2}\right), \qquad \vec{q} = [q_1,\, q_2,\, q_3]^T = \hat{\varphi}\, \sin\left(\frac{\varphi}{2}\right), \tag{S19}$$

and the absolute rotation vector is

$$\vec{\varphi} = \frac{2\arccos(q_0)}{\sqrt{1-q_0^2}}\,\vec{q}. \tag{S20}$$

Equation (S20) is exact for a single finite rotation, but becomes numerically ill-conditioned when $\|\vec{q}\| = \sqrt{1-q_0^2} \to 0$, which occurs whenever the accumulated polarization rotation approaches an integer multiple of 2π. This is the fundamental origin of the wrapping singularities that motivate the differential quaternion formulation described in Supplementary Note S5. In practice, Eq. (S20) is evaluated stably using a small-angle fallback: when $\|\vec{q}\| < \epsilon_{\mathrm{tol}}$ for a numerical tolerance $\epsilon_{\mathrm{tol}} \approx 10^{-7}$, the rotation vector is approximated as $\vec{\varphi} \approx 2\vec{q}$.

S4 Effect of Disjoint and Joint Carrier Phase Estimation

In disjoint CPE, the x- and y-polarization tributaries are tracked by independent phase loops, as defined by Eq. (S11) of Supplementary Note S2. Because both loops are driven by independent realizations of the Amplified Spontaneous Emission (ASE) noise, they accumulate different phase errors over time. The resulting artificial differential phase is

$$\Delta\phi_{\mathrm{CPE}} = \phi_x - \phi_y, \tag{S21}$$

where ϕ_x and ϕ_y are the phase corrections applied to the x- and y-polarization outputs respectively. This differential phase is not a physical polarization rotation; it is an artifact of independent tracking and does not represent a change in the fiber birefringence.

Small-angle regime

For small deviations around a stable polarization state, the Jones matrix can be linearized. In this regime, the differential carrier-phase error couples primarily into the first Stokes rotation component, producing a perturbed rotation vector of the form [3]

$$\vec{\varphi}' \simeq \vec{\varphi} + \Delta\phi_{\text{CPE}}\,\hat{e}_1, \tag{S22}$$

where $\hat{e}_1$ is the unit vector along the S_1 axis of Stokes space. The differential phase error thus appears as an additive random walk along S_1 that is statistically independent of the physical polarization perturbation. In simulations, Fig. S1 (a), this artifact is visible as an inflated and non-stationary noise floor in the φ_1 component of the rotation vector, while the φ_2 and φ_3 components are relatively unaffected. As shown in Fig. S1 (b), the adoption of a joint CPE structurally forces the differential phase error term $\Delta\phi_{CPE}$ to zero. Consequently, the artificial random walk is entirely eliminated, and the extracted rotation vector components remain stable and quiet around their baseline values. Finally, the causal link between the independent phase recovery loops and the sensing degradation is mathematically proven by the normalized cross-correlation function between the φ_1 drift and the disjoint CPE differential phase $\Delta\phi_{CPE}$ (Fig. S1 (c)). The correlation function exhibits a correlation peak of unity at strictly zero lag. This overlap further confirms that the observed instability is not a physical property of the transmission medium, but a purely algorithmic artifact directly injected into the sensing observable by the disjoint processing of the polarization channels, as predicted in [4].

Dynamic Tracking Regime with ASE-Induced Perturbations and Phase Noise

To evaluate the MIMO-CPE interplay under macroscopic transients, we simulate a uniform polarization rotation driven by a constant rotor at frequency $f_{\text{rot}} = 1$ KHz strictly aligned with the S_2 axis ($\hat{\varphi} = \hat{e}_2$) in the presence of ASE (with SNR = 20 dB) linewidth $\Delta\nu = 100$ kHz. Under large-signal conditions, the small-deviation approximation, expressed in Eq. S22, is invalid, requiring the exact analytical mapping. Following the approach described in the Appendix of [3], by substituting the physical rotation axis $\hat{\varphi} = \hat{e}_2$ and exploiting the cross-product relation $\hat{e}_2 \times \hat{e}_1 = -\hat{e}_3$, the spatial projections of the tracked quaternion components along the Stokes axes are explicitly defined as

$$q_0' = \cos\left(\frac{\varphi}{2}\right)\cos\left(\frac{\Delta\phi_{\text{CPE}}}{2}\right), \tag{S23}$$

$$q_1' = \cos\left(\frac{\varphi}{2}\right)\sin\left(\frac{\Delta\phi_{\text{CPE}}}{2}\right), \tag{S24}$$

$$q_2' = \sin\left(\frac{\varphi}{2}\right)\cos\left(\frac{\Delta\phi_{\text{CPE}}}{2}\right), \tag{S25}$$

$$q_3' = -\sin\left(\frac{\varphi}{2}\right)\sin\left(\frac{\Delta\phi_{\text{CPE}}}{2}\right). \tag{S26}$$

These relations show that the differential phase error creates bounded but potentially significant leakage from the intended S_2-axis rotation into the S_1 and S_3 components. Specifically, the artifacts on the orthogonal axes are multiplicatively governed by $\sin(\Delta\phi_{\mathrm{CPE}}/2)$ inside Eqs. S24 and S26. As long as the disjoint CPE maintains a proper lock, the differential phase error remains relatively small. Consequently, the orthogonal leakage never diverges but appears as a constrained noise envelope modulated by the physical macroscopic rotation terms $\cos(\varphi/2)$ and $\sin(\varphi/2)$ in Fig. S1 (d). Conversely, the adoption of a joint CPE architecture, Fig. S1 (e), structurally forces the differential phase error to identically zero ($\Delta\phi_{\mathrm{CPE}} = 0$). Consequently, the algorithmic cross-talk is entirely extinguished, and the orthogonal tracking parameters φ_1 and φ_3 remain flat at zero, affected only by the baseline isotropic ASE noise.

Joint CPE Suppression

Joint CPE, defined in Eq. (S12) of Supplementary Note S2, applies a common phase correction $f_{\mathrm{ave}} = (f_x + f_y)/2$ to both polarization tributaries. To first order, this halves the residual differential phase to $\Delta\phi_{\mathrm{CPE}}^{\mathrm{joint}} = (f_x - f_y)/2$, and for balanced ASE conditions it suppresses the differential drift by approximately 6 dB relative to disjoint CPE. In the limit of perfectly correlated phase fluctuations, joint CPE eliminates the differential drift entirely. The simulation results comparing disjoint and joint CPE are shown in Fig. S1, reproduced from the main text for completeness, where the inflated noise floor and non-physical random walk in φ_1 under disjoint CPE is clearly visible, and joint CPE restores a flat, isotropic noise floor.

S5 Quaternion Differential Method for Continuous State of Polarization (SOP) Tracking

The SOP extracted from coherent-transponder Jones-matrix telemetry evolves on the special unitary group $SU(2)$. Although an instantaneous Jones matrix can be mapped to an absolute rotation vector in Stokes space using the procedure of Supplementary Note S3, this absolute representation presents two fundamental difficulties for continuous sensing. First, rotations in $SU(2)$ are non-commutative, so the absolute rotation vector associated with the final Jones matrix is not generally equal to the linear accumulation of all local birefringence perturbations along the fiber. Second, absolute rotation coordinates are topologically bounded and become numerically ill-conditioned near integer multiples of 2π, as shown by the denominator of Eq. (S20). A physically continuous polarization trajectory can therefore appear discontinuous when represented by absolute angles, introducing wrapping artifacts into filtered time series and spectrograms.

To avoid both difficulties, we use a differential quaternion formulation that processes only the incremental rotation between consecutive Jones-matrix estimates, maps this increment into the locally Euclidean tangent space of $SU(2)$, and then accumulates the resulting differential rotation vectors as a continuous Cartesian trajectory. The conceptual geometry of this mapping is illustrated in Fig. S2. Interested readers are encouraged to read [5].

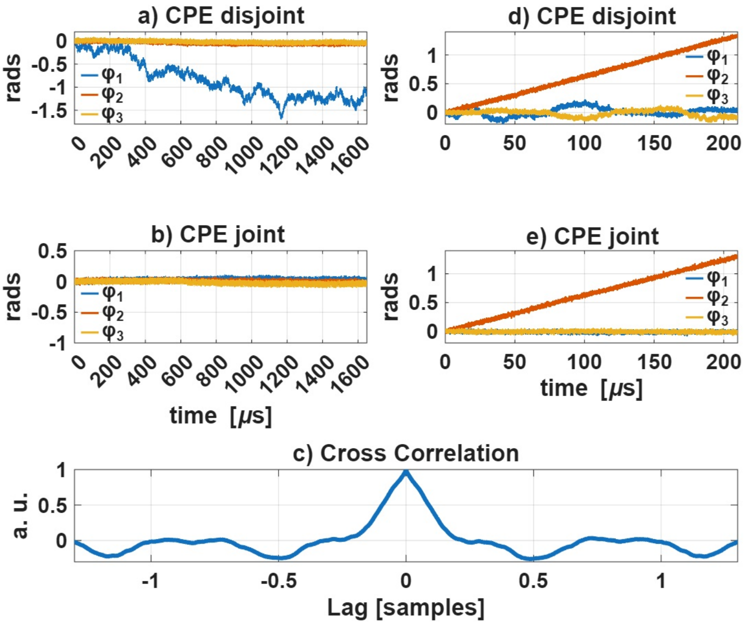

Fig. S1 DSP-induced carrier-phase artifacts in polarization sensing. Numerical simulations comparing disjoint and joint CPE architectures. **(a)** Rotation-vector under disjoint CPE: the φ_1 component exhibits a strongly elevated and frequency-dependent noise floor caused by the artificial differential phase $\Delta\phi_{\mathrm{CPE}}$ accumulating independently in the two polarization phase-tracking loops. **(b)** Rotation-vector under joint CPE: the common phase correction defined in Eq. (S12) suppresses the differential drift, restoring a flat, isotropic estimation-noise floor across all three rotation-vector components. **(d)** As in **(a)** with a uniform polarization rotation driven by a constant rotor at frequency $f_{\mathrm{rot}} = 1$ KHz strictly aligned with the S_2 axis and disjoint CPE. **(e)** As in **(d)** with CPR joint. **(c)** Stokes angles with CPE joint phase estimation. The simulation parameters are: 16-QAM at 12 Gbaud, combined laser linewidth $\Delta\nu = 100$ kHz.

Unit Quaternion Representation

Starting from the $SU(2)$-normalized Jones matrix U' extracted via the procedure of Supplementary Note S3, the unit quaternion at telemetry sample k is defined as

$$\mathbf{Q}_k = \begin{bmatrix} q_{0,k} \\ \vec{q}_k \end{bmatrix} = \begin{bmatrix} q_{0,k} \\ q_{1,k} \\ q_{2,k} \\ q_{3,k} \end{bmatrix}, \qquad \|\mathbf{Q}_k\|^2 = q_{0,k}^2 + \|\vec{q}_k\|^2 = 1, \tag{S27}$$

where $q_{0,k}$ is the scalar part and $\vec{q}_k = [q_{1,k}, q_{2,k}, q_{3,k}]^T$ is the vector part at sample k. The quaternion components are related to the $SU(2)$ matrix elements by Eq. (S18), and the corresponding absolute rotation angle and axis are given by Eq. (S19).

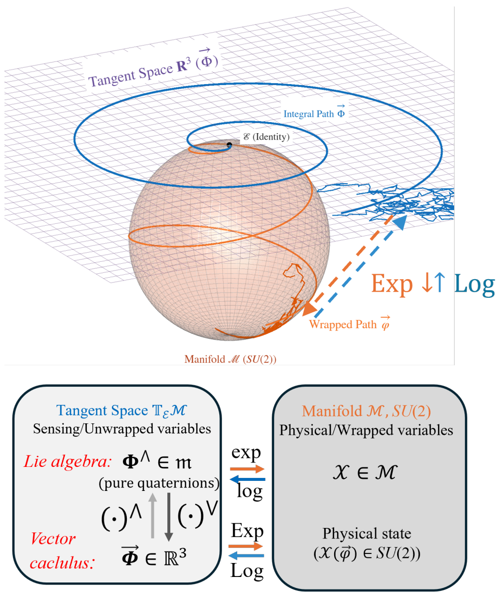

Fig. S2 Conceptual Lie-group mapping for continuous polarization tracking. Absolute polarization states evolve on the curved $SU(2)$ manifold $\mathcal{M}$, where finite rotations can suffer from 2π wrapping and coordinate singularities near the principal-domain boundaries (indicated by the dashed boundary circle). The differential quaternion method instead maps only the incremental rotation $\Delta\mathbf{Q}_k$ between consecutive samples into the locally flat tangent space $\mathbb{R}^3$ at the identity element, where the accumulated sensing variable can be integrated and processed using standard linear signal-processing tools without topological constraints.

Incremental Quaternion via the Hamilton Product

Instead of evaluating Eq. (S20) at each sample, we compute the relative rotation between consecutive samples. The incremental quaternion is obtained via the Hamilton product

$$\Delta\mathbf{Q}_k = \mathbf{Q}_k \otimes \mathbf{Q}_{k-1}^{-1}, \tag{S28}$$

where the inverse (conjugate) of the previous unit quaternion is

$$\mathbf{Q}_{k-1}^{-1} = \begin{bmatrix} q_{0,k-1} \\ -\vec{q}_{k-1} \end{bmatrix}. \tag{S29}$$

Expanding the Hamilton product yields the scalar and vector parts of $\Delta\mathbf{Q}_k$:

$$q_{0,\Delta} = q_{0,k}\, q_{0,k-1} + \vec{q}_k \cdot \vec{q}_{k-1}, \tag{S30}$$

$$\vec{v}_\Delta = q_{0,k-1}\, \vec{q}_k - q_{0,k}\, \vec{q}_{k-1} - \vec{q}_k \times \vec{q}_{k-1}. \tag{S31}$$

The incremental quaternion $\Delta\mathbf{Q}_k = [q_{0,\Delta},\, \vec{v}_\Delta^T]^T$ satisfies $\|\Delta\mathbf{Q}_k\|^2 = 1$ by construction and represents the rotation that maps the polarization state at sample $k-1$ to that at sample k.

Mapping to the Lie algebra

The incremental quaternion is next mapped into the Lie algebra of $SU(2)$, which is the tangent space at the identity. Provided the telemetry rate F_s is high relative to the bandwidth of the physical polarization dynamics, each incremental rotation is small and the following four-quadrant inverse-tangent mapping is numerically well-conditioned:

$$\Delta\vec{\Phi}_k = 2\,\mathrm{atan2}(\|\vec{v}_\Delta\|,\ q_{0,\Delta})\,\frac{\vec{v}_\Delta}{\|\vec{v}_\Delta\|}, \tag{S32}$$

where $\mathrm{atan2}(y, x)$ is the four-quadrant arctangent that returns values in $(-\pi, \pi]$. In the limit $\|\vec{v}_\Delta\| \to 0$, Eq. (S32) is evaluated using the small-angle approximation to avoid numerical division by zero:

$$\Delta\vec{\Phi}_k \simeq 2\vec{v}_\Delta, \qquad \|\vec{v}_\Delta\| < \epsilon_{\mathrm{tol}}. \tag{S33}$$

The differential rotation vector $\Delta\vec{\Phi}_k \in \mathbb{R}^3$ is the tangent-space representation of the incremental polarization change between samples $k-1$ and k. Its three components correspond to infinitesimal rotations around the S_1, S_2, and S_3 Stokes axes respectively.

Discrete-time integration and baseline removal

The continuous unwrapped polarization trajectory is obtained by discrete-time cumulative summation of the differential rotation vectors:

$$\vec{\Phi}_k = \vec{\Phi}_{k-1} + \Delta\vec{\Phi}_k, \qquad \vec{\Phi}_0 = \vec{0}. \tag{S34}$$

The accumulated trajectory $\vec{\Phi}_k \in \mathbb{R}^3$ is distinct from the bounded absolute rotation vector $\vec{\varphi}_k$ of Eq. (S20). It is an unrolled, topologically unconstrained representation of the polarization evolution and can therefore be processed using any standard linear digital signal-processing operation without concern for wrapping or boundary effects. Slow polarization drift is removed by subtracting a moving-average baseline of appropriate duration from $\vec{\Phi}_k$, as described in Methodology Section 4.2. Seismic-band signals are then isolated by high-pass or band-pass filtering the baseline-subtracted trajectory.

Numerical Validation

To demonstrate the advantage of the differential method over absolute-angle tracking, we performed a numerical stress test in which the SOP was forced to rotate continuously around the S_2 axis at $100\,\mathrm{krad\,s^{-1}}$, with a combined laser linewidth of 100 kHz and a received SNR = 20 dB. The results are shown in Fig. S3.

As shown in Fig. S3(b), the absolute-angle formulation of Eq. (S20) exhibits sharp singular spikes at each 2π crossing point. These spikes alias into the signal band during filtering and produce spurious spectral lines that can obscure genuine seismic signals. In contrast, the differential quaternion method in Fig. S3(c) tracks only the infinitesimal increments and integrates them in the tangent space, producing a continuous, artifact-free trajectory regardless of the accumulated rotation. Beyond

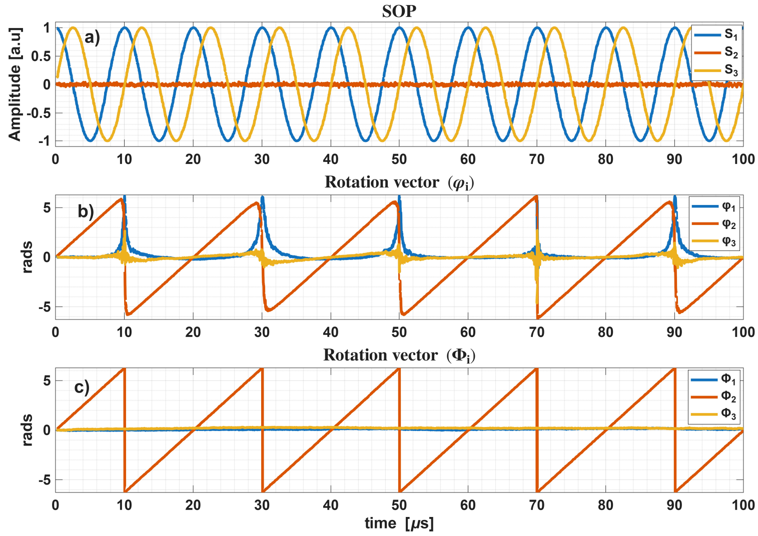

Fig. S3 Numerical validation of the quaternion differential method under continuous rotation. (a) Simulated SOP trajectory under continuous rotation around the S_2 axis at 100 krad s^{-1} with combined laser linewidth 100 kHz and SNR = 20 dB. **(b)** Absolute rotation angles extracted via Eq. (S20): singular spikes appear near every integer multiple of 2π where the denominator $\|\vec{q}\| \to 0$, rendering the absolute representation unsuitable for continuous sensing or spectral analysis. **(c)** Integrated tangent-space trajectory obtained using Eqs. (S32) and (S34): the differential quaternion method produces a smooth, continuous signal free of wrapping artifacts, demonstrating its suitability for real-time filtering and spectral estimation.

eliminating wrapping singularities, the differential formulation reduces computational load: the integration step in Eq. (S34) requires only vector additions, avoiding the matrix inversions and trigonometric evaluations that are repeated at every sample in the absolute-angle pipeline. Numerical timing benchmarks confirm an execution-time reduction of approximately 58% relative to the classical absolute-rotation method for the sampling rates used in this study.

S6 Principal Component Analysis (PCA) for anisotropic noise suppression

Let $\vec{\Phi}_k \in \mathbb{R}^3$ denote the baseline-subtracted rotation-vector time series at telemetry sample k, obtained from the differential quaternion integration of Supplementary Note S5. Over a selected noise estimation window of N_{noise} samples, the sample covariance matrix of the rotation vector is

$$\mathbf{C}_{\text{noise}} = \frac{1}{N_{\text{noise}} - 1} \sum_{k=1}^{N_{\text{noise}}} \left(\vec{\Phi}_k - \bar{\vec{\Phi}}\right) \left(\vec{\Phi}_k - \bar{\vec{\Phi}}\right)^T, \tag{S35}$$

where $\bar{\vec{\Phi}} = N_{\text{noise}}^{-1} \sum_k \vec{\Phi}_k$ is the sample mean over the noise window. An analogous covariance matrix $\mathbf{C}_{\text{signal}}$ is computed over the 2 min signal window centered on the peak polarization response. Both covariance matrices are symmetric positive semi-definite 3×3 matrices.

The eigendecomposition of the noise covariance matrix is

$$\mathbf{C}_{\text{noise}} = \mathbf{V}\,\mathbf{\Lambda}\,\mathbf{V}^T, \tag{S36}$$

where $\mathbf{V} = [\vec{v}_1, \vec{v}_2, \vec{v}_3]$ is the orthonormal matrix of eigenvectors and $\mathbf{\Lambda} = \text{diag}(\lambda_1, \lambda_2, \lambda_3)$ contains the eigenvalues ordered such that $\lambda_1 \geq \lambda_2 \geq \lambda_3 \geq 0$. Each eigenvector $\vec{v}_i$ defines a principal direction of the background noise in Stokes space; the corresponding eigenvalue λ_i is the noise variance projected onto that direction.

The rotation-vector time series is projected into the principal-component basis by

$$\tilde{\vec{\Phi}}_k = \mathbf{V}^T\,\vec{\Phi}_k, \tag{S37}$$

yielding three scalar time series $\tilde{\Phi}_{k,i} = \vec{v}_i^T \vec{\Phi}_k$ for $i = 1, 2, 3$. In this basis, the noise covariance matrix is diagonal by construction:

$$\mathbf{V}^T\,\mathbf{C}_{\text{noise}}\,\mathbf{V} = \mathbf{\Lambda}. \tag{S38}$$

The signal-to-noise ratio for component i is estimated as

$$\text{SNR}_i = \frac{(\mathbf{V}^T\,\mathbf{C}_{\text{signal}}\,\mathbf{V})_{ii}}{\lambda_i}, \tag{S39}$$

and the component with the highest SNR_i is selected for further seismic analysis. When the noise is anisotropic—that is, when $\lambda_1 \gg \lambda_2$ or $\lambda_1 \gg \lambda_3$—and the earthquake signal projects substantially onto the low-noise principal directions, this rotation provides a meaningful improvement in detectability relative to any fixed Cartesian axis. When the noise covariance is approximately isotropic ($\lambda_1 \approx \lambda_2 \approx \lambda_3$), the principal-component basis provides no advantage over the original coordinate system, as observed for the CAT01 transponder in Fig. 8 of the main text.

For Subcarrier (SC) fusion, N_{sc} subcarrier rotation-vector estimates $\{\vec{\Phi}_k^{(j)}\}_{j=1}^{N_{sc}}$ are first aligned into a common reference frame by estimating and removing a subcarrier-specific mean rotation from a short calibration window. The fused estimate is then formed as the arithmetic mean:

$$\vec{\Phi}_k^{\text{fused}} = \frac{1}{N_{sc}} \sum_{j=1}^{N_{sc}} \vec{\Phi}_k^{(j)}. \tag{S40}$$

Under the assumption that the physical polarization perturbation is identical across subcarriers while the estimation noise contributions $\{\vec{n}_k^{(j)}\}$ are zero-mean and mutually uncorrelated, the noise variance of the fused estimate is reduced by a factor of N_{sc}

relative to any single subcarrier:

$$\mathrm{Var}\left[\vec{\Phi}_k^{\mathrm{fused}}\right] = \frac{1}{N_{sc}} \mathrm{Var}\left[\vec{\Phi}_k^{(1)}\right], \tag{S41}$$

while the physical signal component is preserved at full amplitude. This result is consistent with the approximately eightfold noise PSD reduction observed in the laboratory measurements with eight subcarriers, as shown in Fig. 7 of the main text. The reduction is achieved only for uncorrelated noise components; correlated fluctuations arising from the shared optical path are not suppressed by fusion, which explains the diminishing benefit of SC averaging observed at minute-to-hour timescales.

References

[1] Czegledi, C.B., Karlsson, M., Agrell, E., Johannisson, P.: Polarization drift channel model for coherent fibre-optic systems. Scientific reports **6**(1), 21217 (2016)

[2] Mori, Y., Zhang, C., Kikuchi, K.: Novel configuration of finite-impulse-response filters tolerant to carrier-phase fluctuations in digital coherent optical receivers for higher-order quadrature amplitude modulation signals. Opt. Express **20**(24), 26236–26251 (2012) https://doi.org/10.1364/OE.20.026236

[3] Mecozzi, A., *et al.*: Use of optical coherent detection for environmental sensing. Journal of Lightwave Technology **41**(11), 3350–3357 (2023)

[4] Mecozzi, A., *et al.*: Use of optical coherent detection for environmental sensing. In: European Conference on Optical Communication (ECOC) 2022, pp. 3–1. Optica Publishing Group, ??? (2022). https://doi.org/10.1364/ECEOC.2022.Tu3D.1 . https://opg.optica.org/abstract.cfm?URI=ECEOC-2022-Tu3D.1

[5] Kuipers, J.: Quaternions and rotation sequences: A primer with applications to orbits, aerospace and virtual reality. (2002). https://api.semanticscholar.org/CorpusID:283566449